Transition kinetics of defect patterns in confined two-dimensional smectic liquid crystals

Xiao-Jie Zhang, Yu-Wei Sun, Zhan-Wei Li [●],[*] and Zhao-Yan Sun
State Key Laboratory of Polymer Physics and Chemistry,
Changchun Institute of Applied Chemistry, Chinese Academy of Sciences, Changchun 130022, China
and University of Science and Technology of China, Hefei 230026, China

Topological defects in liquid crystals under confined geometries have attracted extensive research interests. Here, we perform molecular dynamics simulations to investigate the formation and transition of defect patterns in two-dimensional smectic Gay-Berne liquid crystals with a simple rectangular confinement boundary. Two typical types of defect patterns, bridge and diagonal defect patterns, are observed, which can be transformable continuously between each other over time. The transition usually starts from the line or point defect regions, and the competition between neighboring and opposite boundary effects induces the continuous realignments of the smectic layers to connect the neighboring or opposite walls. The relative stability of these two defect patterns can be controlled by changing the confinement conditions. These results deepen our understanding of transition kinetics of defect patterns in confined liquid crystals.

I. INTRODUCTION

Liquid crystals are a fascinating category of soft matter systems, which combine the fluidity of liquids and the long-range orientational order feature of crystalline solids [1]. The orientational order and mobility of liquid crystal molecules provide the possibility of realizing novel liquid crystal materials with unique properties [2–8]. In fact, confined liquid crystals are commonly encountered in scientific research and practical applications [9–27]. Due to the subtle balance between bulk elasticity and boundary anchoring, the confinement will disrupt the uniform orientational patterns and impose complex frustration on liquid crystal order, and then lead to a rich variety of topological defects [11,22–24,28–31]. These topological defects have a significant influence on the macroscopic properties of liquid crystal materials [28–33]. Furthermore, defects in liquid crystals can be used as a very valuable model system to study the topological defects in diverse disciplines, including condensed matter physics [34], biology [35], and cosmology [36].

Driven by the use of nematics in display technologies, the confinement of the nematic phase has been a subject of much interest in recent years [11,13,19,37–41]. How defect patterns in nematic phase can be influenced by various factors, including liquid crystal molecules [37–40], sizes and geometries of confinement boundary [10,11,22,41], and anchoring conditions [13,19,23,39], have been extensively investigated. Nevertheless, it is worth mentioning that the smectic phase with multistable electro-optic effect [42–44] could also be applied to flexible displays [45] and memory devices [46]. Furthermore, the smectic phase exists in many biological systems, such as viruses [47], vesicles [48], and gapped DNA

duplexes [49]. In square-confined smectics, bridge defect patterns have been found by density-functional theory [9] and Monte Carlo simulation [50]. Diagonal defect patterns have also been observed in experiment [24]. However, most of these works have mainly focused on the static properties of defect patterns; very little work has focused on the dynamical properties of defect patterns and their transition kinetics [51].

In this work, we will focus on understanding and controlling the transition kinetics of defect patterns in two-dimensional (2D) smectic liquid crystals confined in a simple rectangular boundary, which can capture the essential features of more complicated liquid-crystal confinement problems [11,52,53]. Based on the Gay-Berne (GB) potential model, 2D liquid crystals composed of elliptical particles are systematically studied by means of molecular dynamics simulations both in the bulk state and under confinement. In agreement with the experiment [24], two typical types of defect patterns, bridge and diagonal defect patterns, are observed. Our simulation results further reveal that these two defect patterns can be transformable continuously between each other over time. The transition usually starts from the line or point defect regions, and the competition between neighboring and opposite boundary effects induces the continuous realignments of the smectic layers to connect the neighboring or opposite walls. To address how to control the relative stability of these two defect states, we also explore the impacts of the box-ellipse size ratio, the aspect ratio of the confinement rectangle, and the strength of parallel surface anchoring interaction on the probabilities for appearance of these defect patterns.

II. MODEL AND SIMULATION DETAILS

In this work, the coarse-grained liquid crystal molecules are confined in a two-dimensional rectangle, whose boundary is composed of Lennard-Jones (LJ) particles. A schematic
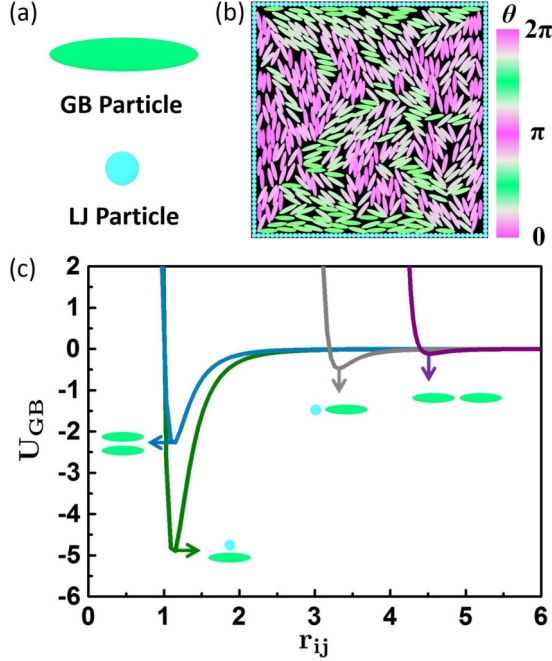
FIG. 1. (a) Graphical representations of the GB-type elliptical particle and LJ-type wall particle. (b) Schematic depiction of the simulation system. The particles are colored according to the angle θ between the major axis of elliptical particles and the Y axis. (c) The interaction potential U_{GB} (in units of ϵ_0) of elliptical particles and wall particles as a function of separation r_{ij} (in units of σ_0) for side-by-side and end-to-end configurations when $\epsilon_{GB\text{-}GB} = 1.0\epsilon_0$ and $\epsilon_{GB\text{-}LJ} = 5.0\epsilon_0$.

representation of the system is given in Fig. 1. Our systems consist of 119 to 1606 liquid crystal molecules, which are described as elliptical particles via the GB potential model [54], depending on the size and the aspect ratio of confinement rectangles. Each elliptical particle is characterized by its semiaxis lengths a_i, b_i and well depths ϵ_{ia}, ϵ_{ib} for side-by-side and end-to-end interactions. All the simulation parameters are described in dimensionless units in terms of the characteristic mass m_0, length σ_0, energy ϵ_0, and the time unit $\tau = \sigma_0 (m_0/\epsilon_0)^{1/2}$. Ellipse-ellipse interactions are given by

$$U_{GB}(\mathbf{A}_i, \mathbf{A}_j, \mathbf{r}_{ij}) = U_r(\mathbf{A}_i, \mathbf{A}_j, \mathbf{r}_{ij})\eta(\mathbf{A}_i, \mathbf{A}_j)\chi(\mathbf{A}_i, \mathbf{A}_j, \mathbf{r}_{ij}),$$
(1)

where $\mathbf{r}_{ij}$ is the interparticle vector between particles i and j, and $U_r(\mathbf{A}_i, \mathbf{A}_j, \mathbf{r}_{ij})$ controls the shifted distance dependence of the interaction:

$$U_r(\mathbf{A}_i, \mathbf{A}_j, \mathbf{r}_{ij}) = 4\epsilon \left[\left(\frac{\sigma}{h_{ij} + \gamma\sigma} \right)^{12} - \left(\frac{\sigma}{h_{ij} + \gamma\sigma} \right)^6 \right].$$
(2)

Here, $h_{ij}(\mathbf{A}_i, \mathbf{A}_j, \mathbf{r}_{ij}) = r_{ij} - \sigma_{ij}(\mathbf{A}_i, \mathbf{A}_j, \mathbf{r}_{ij})$ is the distance of closest approach between two elliptical particles, γ is the shift parameter, $\sigma_{ij}(\mathbf{A}_i, \mathbf{A}_j, \mathbf{r}_{ij}) = [\frac{1}{2}\hat{\mathbf{r}}_{ij}^T \mathbf{G}_{ij}^{-1}(\mathbf{A}_i, \mathbf{A}_j)\hat{\mathbf{r}}_{ij}]^{-1/2}$, $r_{ij} = |\mathbf{r}_{ij}|$ is the center-to-center distance between particles i and j, $\hat{\mathbf{r}}_{ij} = \mathbf{r}_{ij}/r_{ij}$ is a unit vector, and $\mathbf{A}_i$ is the rotation matrix from the space frame to the body frame, which is generated by the normalized quaternion $\mathbf{q}_i = (q_{i,0}, q_{i,1}, q_{i,2}, q_{i,3})$. According to the diagonal shape matrices

$\mathbf{S}_i = \text{diag}(a_i, b_i)$ and $\mathbf{S}_j = \text{diag}(a_j, b_j)$, the symmetric overlap matrix $\mathbf{G}_{ij}(\mathbf{A}_i, \mathbf{A}_j)$ can be defined as $\mathbf{G}_{ij}(\mathbf{A}_i, \mathbf{A}_j) = \mathbf{A}_i^T \mathbf{S}_i^2 \mathbf{A}_i + \mathbf{A}_j^T \mathbf{S}_j^2 \mathbf{A}_j$.

In Eq. (1), $\eta(\mathbf{A}_i, \mathbf{A}_j)$ and $\chi(\mathbf{A}_i, \mathbf{A}_j, \mathbf{r}_{ij})$ control the anisotropic interaction strength based on the relative orientation and position of the elliptical particles:

$$\eta(\mathbf{A}_i, \mathbf{A}_j) = \left[\frac{2 s_i s_j}{\det[\mathbf{G}_{ij}(\mathbf{A}_i, \mathbf{A}_j)]} \right]^{\nu/2},$$
(3)

where

$$s_i = (a_i b_i)^{3/2};$$
(4)

and

$$\chi(\mathbf{A}_i, \mathbf{A}_j, \mathbf{r}_{ij}) = \left[2\hat{\mathbf{r}}_{ij}^T \mathbf{B}_{ij}^{-1}(\mathbf{A}_i, \mathbf{A}_j)\hat{\mathbf{r}}_{ij} \right]^\mu,$$
(5)

where $\mathbf{B}_{ij}(\mathbf{A}_i, \mathbf{A}_j) = \mathbf{A}_i^T \mathbf{E}_i \mathbf{A}_i + \mathbf{A}_j^T \mathbf{E}_j \mathbf{A}_j$ is defined in terms of the diagonal interaction matrices $\mathbf{E}_i = \text{diag}((\epsilon_0/\epsilon_{ia})^{1/\mu}, (\epsilon_0/\epsilon_{ib})^{1/\mu})$ and $\mathbf{E}_j = \text{diag}((\epsilon_0/\epsilon_{ja})^{1/\mu}, (\epsilon_0/\epsilon_{jb})^{1/\mu})$. The parameters μ and ν are empirical exponents that can be used to tune the potential.

The elliptical particles used in this work have an aspect ratio of 4.4 [55], which exhibit isotropic, nematic, smectic and crystalline phases in the bulk. This model is often used to describe p-terphenyl in experiments [18,56,57]. The GB parameters in Eqs. (1)–(5) are set as $\epsilon = \epsilon_0$, $\sigma = \sigma_0$, $a_i = \sigma_0$, $b_i = 4.4\sigma_0$, $\epsilon_{ia} = \epsilon_0$, $\epsilon_{ib} = 0.05\epsilon_0$, $\gamma = 1$, $\mu = 1$, $\nu = 1$, and the GB interactions are truncated at the cutoff radius $r_{\text{cut}} = 5.4\sigma_0$. The wall particles are realized by simply setting the GB parameters as $\epsilon = \epsilon_0$, $\sigma = \sigma_0$, $a_i = b_i = \sigma_0$. Moreover, the interactions between wall particles are neglected and the interactions between wall particles and elliptical particles are given as Eq. (1).

We perform molecular dynamics simulations in the NVT ensemble by using the Nosé-Hoover thermostat. The elliptical particles are initially placed randomly in the confinement rectangle, and the number density of elliptical particles is $\rho = 0.19$, which corresponds to the packing fraction $\phi \approx 0.66$. As shown in Fig. S1 of the Supplemental Material [58], at $\rho = 0.19$, the bulk systems can well exhibit isotropic, nematic, and smectic phases in the simulated temperature range, and show higher orientational ordering. The temperature is set as $T^* = k_B T/\epsilon_0 = 16$, which is above the isotropic-nematic phase transition temperature in the bulk. After equilibrating for 1.0×10^6 time steps, the system is cooled down to $T^* = 0.3$ immediately and then kept for 1.0×10^7 time steps, at which the smectic-like structures with certain defect patterns are formed. To investigate the transformation between different defect patterns, we track the whole trajectory of every particle in the simulations [59]. The translational and rotational equations of elliptical particles are integrated using a Velocity-Verlet-like algorithm [54] with a time step $\delta t = 0.001\tau$.

III. RESULTS AND DISCUSSION

A. Phase behavior of elliptical particles in the bulk

We first begin our study with unconfined bulk systems under periodic boundary conditions. To quantitatively identify different liquid crystal phases, the orientational order

parameter S_2, the radial distribution function $g(r)$, the radial distribution function parallel to the director $g_\parallel(r_\parallel)$, and the mean square displacement (MSD) are calculated. The orientational order parameter S_2 is defined as the largest eigenvalue of the order tensor $Q_{\alpha\beta}$ [16]:

$$Q_{\alpha\beta} = \frac{1}{N}\left\langle \sum_{i=1}^{N}[2\mathbf{u}_\alpha(i)\cdot\mathbf{u}_\beta(i) - \delta_{\alpha\beta}]\right\rangle, \qquad (6)$$

where $u_\alpha(i)$ is the αth Cartesian coordinate of the unit vector specifying the orientation of molecule i and $\delta_{\alpha\beta}$ is the Kronecker symbol. The increase of S_2 often suggests the emergence of orientational ordering, and $S_2 = 1$ corresponds to the perfectly orientational ordered structure. The radial distribution function is given by

$$g(r) = \frac{1}{l_x l_y N \rho}\left\langle \sum_{i}^{N}\sum_{j\neq i}^{N}\delta(r - r_{ij})\right\rangle, \qquad (7)$$

where l_x and l_y are the box length along X and Y axes, respectively, and ρ is the number density of elliptical particles. The radial distribution function parallel to the director $g_\parallel(r_\parallel)$, which is sensitive to the arrangement of the elliptical particles within the layers, is described as [60]

$$g_\parallel(r_\parallel) = \frac{1}{l_x l_y N \rho}\left\langle \sum_{i}^{N}\sum_{j\neq i}^{N}\delta(r_\parallel - \mathbf{n}\cdot\mathbf{r}_{ij})\right\rangle, \qquad (8)$$

where $r_\parallel$ is the projection of the interparticle vector $\mathbf{r}_{ij}$ between elliptical particles i and j along the orientation vector $\mathbf{n}$. The mean square displacement (MSD) is evaluated by

$$g_1(t) = \frac{1}{N}\left\langle \sum_{i=1}^{N}[r_i(t) - r_i(0)]^2\right\rangle, \qquad (9)$$

where $r_i(t)$ is the position of the ith elliptical particle at time t. Figure 2 shows the typical snapshots of isotropic (I) phase [Fig. 2(a)], nematic (N) phase [Fig. 2(b)], smectic (Sm) phase [Fig. 2(c)], and solid (S) phase [Fig. 2(d)], together with the corresponding calculated S_2, $g(r)$, $g_\parallel(r_\parallel)$, and MSD. Each system is set to target temperature independently. As shown in Fig. 2, with decreasing temperature, the order parameter S_2 increases in four distinct regions. The isotropic-nematic transition is detected at $T^* \approx 13.0$ where the slope of S_2 changes [61]. The average heat capacity per particle C_V/N is also calculated by $C_V = \frac{\langle\delta U^2\rangle}{k_B T^2} + \frac{3}{2}Nk_B$ [62] and $C_V = (\partial E/\partial T)_V$ [63–65]. As shown in Fig. S2 [58], the values of C_V/N are all around $C_V/N \approx 1.8$, and there is no sharp change. So this isotropic-nematic transition should be continuous. With further decreasing temperature to $T^* \approx 0.7$, the slope of S_2 increases greatly and the smectic phase is identified by the long-ranged peaks of $g_\parallel(r_\parallel)$ with a period of approximately particle length ($b = 4.4$). At $T^* \approx 0.08$, the peaks of $g(r)$ and $g_\parallel(r_\parallel)$ start to become sharp and narrow. We identify this as solid phase and expect that relatively perfect crystal phase will appear at higher number densities. It is clearly seen that the smectic phase shows better orientational ordering [Fig. 2(e)] than the nematic and isotropic phases, and its fluidity is much better than the solid phase [Fig. 2(h)]. Moreover, as shown in Fig. 2(c), no obvious defects could be seen in the smectic
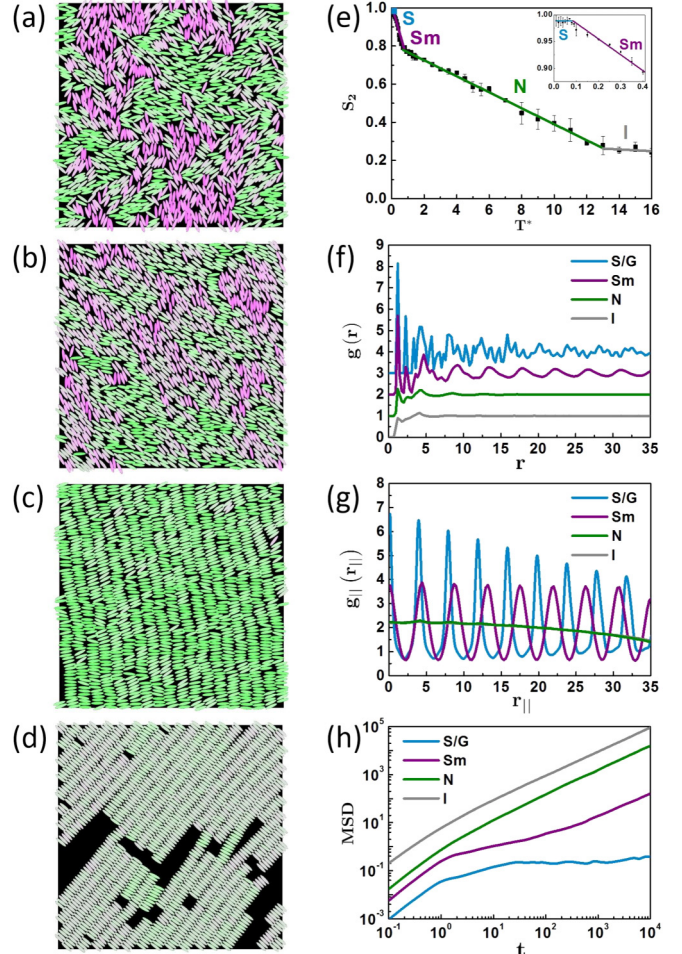

FIG. 2. (a) Isotropic (I) phase at $T^* = 16$, (b) nematic (N) phase at $T^* = 1.0$, (c) smectic (Sm) phase at $T^* = 0.3$, (d) solid (S) phase at $T^* = 0.05$, (e) orientational order parameter S_2 as a function of temperature T^*, and the inset in (e) is a plot enlarging the region near the smectic-solid transition, (f) radial distribution function $g(r)$ of different phases, and curves are shifted vertically for better visualization, (g) radial distribution function parallel to the director $g_\parallel(r_\parallel)$ of different phases, (h) the mean square displacement (MSD) of different phases. The simulations are performed in 2D unconfined bulk system with the box length $W_x = 80\sigma_0$.

phase at $T^* = 0.3$ for the bulk system, and so we choose $T^* = 0.3$ as the state point in the following study to understand the formation of defect patterns in 2D smectic phase under confinement.

B. Defect patterns in confined smectic liquid crystals

Figure 3 shows typical defect patterns in 2D smectic phase under square confinements with the side lengths $W_x = 50\sigma_0$ at $T^* = 0.3$. For comparison, the smectic phase obtained in the bulk system is also given in Fig. 3(a). Due to the parallel surface anchoring interaction, elliptical particles near the walls tend to align parallel to the walls, and other elliptical particles form smectic layers connecting neighboring or opposite walls. In agreement with the experiment [24], two typical types of defect patterns, bridge and diagonal patterns, are observed.
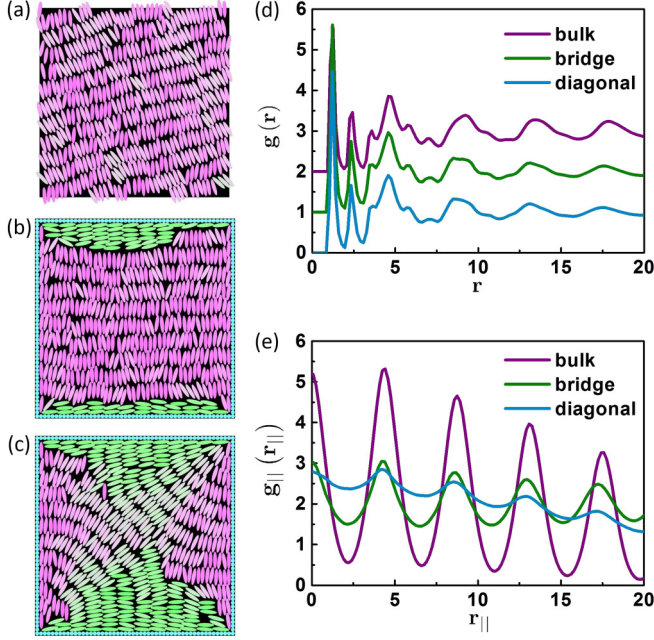
FIG. 3. Typical defect patterns observed at $W_x = 50\sigma_0$ and $T^* = 0.3$: (a) smectic phase in the bulk, (b) bridge defect pattern, and (c) diagonal defect pattern. (d) Radial distribution function $g(r)$ of these structures; curves are shifted vertically for better visualization. (e) Radial distribution function parallel to the director $g_\parallel(r_\parallel)$ of these structures.

These two defect patterns under square confinements with different side lengths W_x are also given in Fig. S3 [58]. As shown in Fig. 3(b) and Fig. S3 [58], the bridge defect is characterized by three smectic domains. Two small green domains are anchored parallel to two opposite sides, and a large purple domain connects the other two sides. To meet parallel surface anchoring conditions at neighboring walls, the smectic layers can also bend to form the diagonal defect pattern (Fig. 3(c) and Fig. S3 [58]), which consists of two sectors connected by the diagonal of the square boundary. For a quantitative comparison with the bulk system, the radial distribution function $g(r)$ and the radial distribution function parallel to the director $g_\parallel(r_\parallel)$ are also calculated for these bridge and diagonal patterns. As can be seen in Fig. 3(e), the intensity of the peaks in $g_\parallel(r_\parallel)$ of these two defect patterns is obviously weakened. Moreover, as shown in Fig. S4 [58], the orientational order parameter S_2 of these two defect patterns is significantly reduced. This suggests that the geometrical constraint introduced by the square confinement induces a weaker layered and orientational order in these two defect patterns.

C. Transition kinetics between bridge and diagonal defect patterns

In order to quantitatively distinguish these bridge and diagonal defect states at different simulation times, we calculate the parallel orientational order parameter and the diagonal orientational order parameter, which are defined as [16]

$$S_{pd} = \frac{1}{N}\left\langle \sum_{i=1}^{N} \cos(2\theta_i) \right\rangle, \tag{10}$$

where θ_i is the angle between the orientation of ith particle and the director parallel to the boundary $\mathbf{n}_{\text{paral}}$ or the director parallel to the diagonal of the rectangle $\mathbf{n}_{\text{diag}}$. If the parallel orientational order parameter is larger than the diagonal orientational order parameter, the defect state is recognized as the bridge defect. Otherwise, it is recognized as the diagonal defect.

Figures 4(a) and 4(b) (also Fig. S5 [58]) show the time evolutions of the parallel orientational order parameter and the diagonal orientational order parameter, which suggest that the bridge defect state and diagonal defect state can be transformable continuously between each other over time. Typical snapshots during the transition from the bridge defect to the diagonal defect (B–D transition) are given in Fig. 4(a1)–4(a5), which correspond to five typical time points in the B–D transition marked by blue spheres in Fig. 4(a). Beginning with a typical bridge defect state [Fig. 4(a1)], elliptical particles at the line defect region can rotate to form the smectic layers connecting the neighboring walls [Fig. 4(a2)]. Then, as shown in Fig. 4(a3), the smectic layers connecting the opposite walls will be distorted and form the irregular sectors at two corners along the diagonal direction. Next, elliptical particles around the newly formed defect region will reorganize through translation and rotation to form more ordered smectic layers connecting neighboring walls [Fig. 4(a4)]. Finally, the bending smectic layers reorient along the diagonal direction; a typical diagonal defect is observed in Fig. 4(a5). Conversely, the diagonal defect state could also transform into the bridge defect state over time. Typical snapshots during the transition from the diagonal defect to the bridge defect (D–B transition) are given in Figs. 4(b1)–4(b5). As demonstrated in Fig. 4(b1), the smectic layers connecting to neighboring walls around the point defect regions could be cracked due to the thermal fluctuation, and the elliptical particles will realign into the bending smectic layers connecting to the opposite walls [Fig. 4(b2)]. Then, the bending smectic layers connecting to opposite walls become more dominant [Fig. 4(b3)] and more flatted [Fig. 4(b4)]. Finally, the smectic layers reorient along the parallel direction, and form the typical bridge defect pattern [Fig. 4(b5)].

D. Controlling the relative stability of defect patterns

To address how to control the relative stability of these two defect patterns by changing the confinement conditions, we systematically examine the effects of the box-ellipse size ratio W_x/b, the aspect ratio of confinement rectangle W_y/W_x, and the strength of parallel surface anchoring interaction $\epsilon_{GB\text{-}LJ}$ on the relative probabilities for appearance of these defect patterns. The relative probabilities for each point are calculated using five independent simulation runs with the time of 5.5×10^8 time steps.

For the square confinements, as illustrated in Fig. 5, the bridge defect patterns are absolutely dominant when the strength of parallel surface anchoring interaction $\epsilon_{GB\text{-}LJ}$ is
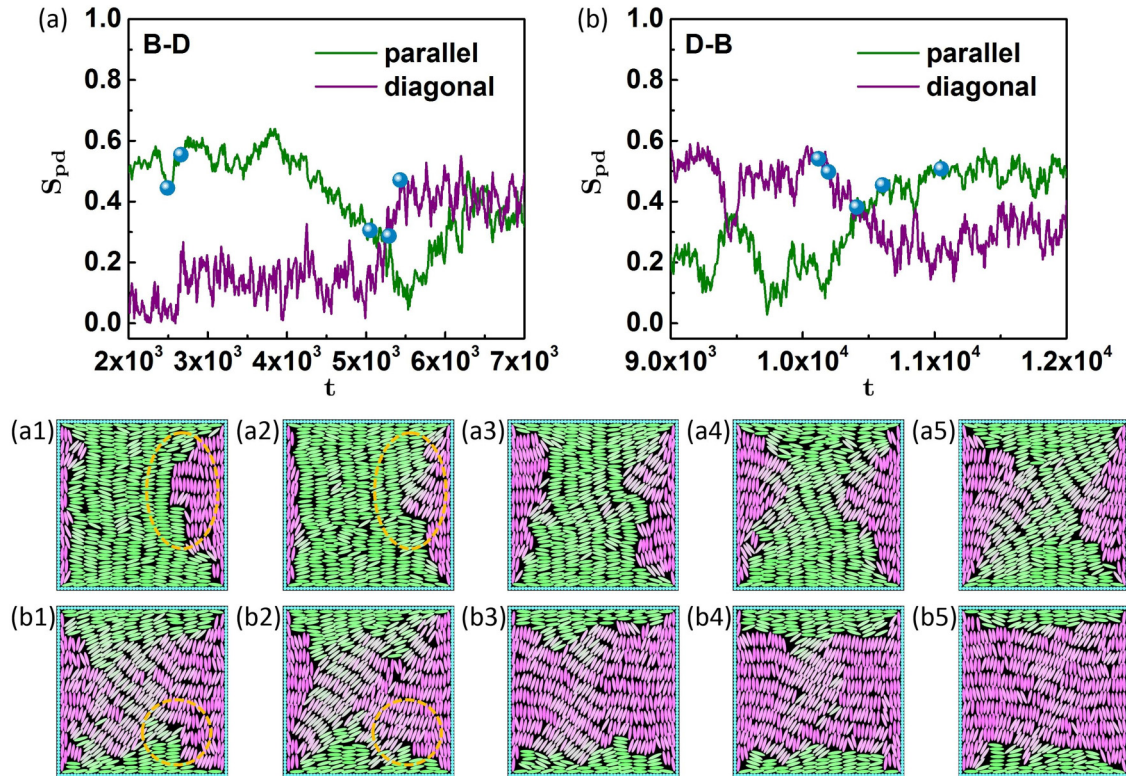
FIG. 4. Transition kinetics between bridge and diagonal defect states at $W_x = 50\sigma_0$ and $\epsilon_{GB\text{-}LJ} = 5.0\epsilon_0$. (a) and (b) Time evolution of the parallel orientational order parameter (green line) and the diagonal orientational order parameter (purple line). (a1)–(a5) Typical snapshots during the transition from the bridge defect to the diagonal defect (B–D). (b1)–(b5) Typical snapshots during the transition from the diagonal defect to the bridge defect (D–B).

small ($\epsilon_{GB\text{-}LJ} = 0.6\epsilon_0$). As $\epsilon_{GB\text{-}LJ}$ increases, the relative probabilities for appearance of diagonal defect patterns become higher. But, when the anchoring strength $\epsilon_{GB\text{-}LJ}$ is larger than $5.0\epsilon_0$, this tendency is no longer apparent. For large values of $\epsilon_{GB\text{-}LJ}$, the probabilities for appearance of diagonal defect patterns also increase upon increasing the box-ellipse size ratio W_x/b. This is because the boundary effects are more profound in a system with small W_x/b, and can influence the structures in the box interior, where the main domain of the

smectic layers aligns parallel to a boundary. For a system with relatively large W_x/b, the defect patterns tend to keep the four-sided symmetry of the original confinement boundaries. So, in comparison with bridge defect patterns, the probabilities for appearance of the diagonal defect patterns are relatively high, and the diagonal defect patterns are more stable.

To further evaluate the relative stability of these two defect patterns, we calculate the free energy differences between them. The bridge defect pattern can transform into the di-
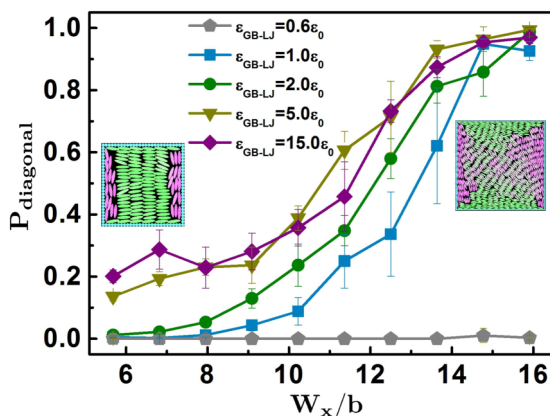

FIG. 5. The relative probabilities for appearance of diagonal defect patterns P_{diagonal} as a function of the box-ellipse size ratio W_x/b at different anchoring strengths $\epsilon_{GB\text{-}LJ}$ in square confinements.
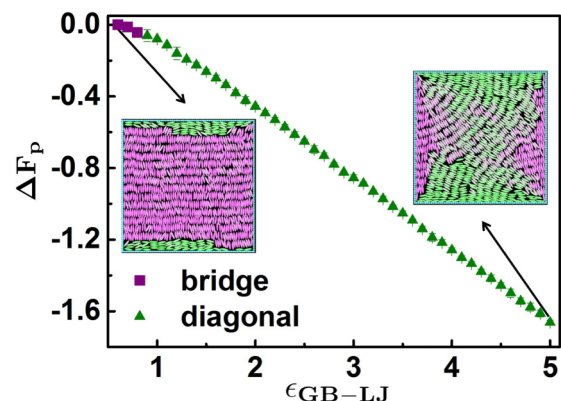

FIG. 6. The free energy differences per particle ΔF_p (in units of $k_B T$) for diagonal defect patterns with respect to the reference bridge defect pattern.
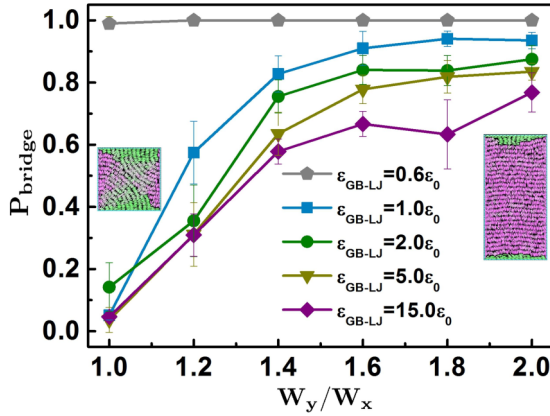
FIG. 7. The relative probabilities for appearance of bridge defect patterns P_{bridge} as a function of the ratio of confinement boundaries W_y/W_x at different anchoring strengths $\epsilon_{GB\text{-}LJ}$ in rectangle confinements while keeping $W_x = 65\sigma_0$.

agonal defect pattern by increasing the strength of parallel surface anchoring interaction $\epsilon_{GB\text{-}LJ}$ at $W_x = 70\sigma_0$. Thus, the free energy differences of diagonal defect pattern with respect to the reference bridge defect pattern can be calculated by thermodynamic integration [66,67]. The integrating equation can be expressed as $F(\epsilon_{GB\text{-}LJ,\mathrm{diagonal}}) - F(\epsilon_{GB\text{-}LJ,\mathrm{bridge}}) = \int_{\epsilon_{GB\text{-}LJ,\mathrm{bridge}}}^{\epsilon_{GB\text{-}LJ,\mathrm{diagonal}}} d\epsilon_{GB\text{-}LJ} \langle \frac{\partial U(\epsilon_{GB\text{-}LJ})}{\partial \epsilon_{GB\text{-}LJ}} \rangle_{\epsilon_{GB\text{-}LJ}}$, where $\langle \cdots \rangle_{\epsilon_{GB\text{-}LJ}}$ denotes an ensemble average for a system with a potential function $U(\epsilon_{GB\text{-}LJ})$. Figure 6 shows the free energy differences per particle ΔF_p for diagonal defect patterns with the bridge defect pattern as the reference measured with the increasing rate of $\Delta\epsilon_{GB\text{-}LJ} = 0.1$ per 1.0×10^7 time steps. The calculated results are not affected by different increasing rates of $\Delta\epsilon_{GB\text{-}LJ}$ (Fig. S6 [58]). As $\epsilon_{GB\text{-}LJ}$ increases, the diagonal defect patterns become more stable, which is consistent with the relative probabilities for appearance of the diagonal defect patterns in Fig. 5. All the free energy differences per particle of these defect patterns range from $-1.66k_BT$ to $0.00k_BT$, which are low enough to allow the continuous transformation between bridge and diagonal defect patterns over time.

As shown in Fig. 7 and Fig. S7 [58], the relative probabilities for appearance of these two defect patterns are also affected by the shape of confinement boundaries. The align-

ment of elliptical particles near the two ends of the rectangular boundary is similar to that of the square boundary, while the elliptical particles near the middle region align along the long side direction. So, as the aspect ratio of confinement rectangle W_y/W_x increases, more stable defect pattern is the bridge one, whose symmetry is inherited from the rectangular boundary. As for the middle region, whose width is $W_y - W_x$, the smectic layers are connected to the opposite walls because the distance from elliptical particles to the opposite walls is closer than the one from elliptical particles to the adjacent walls. Hence, The proportion of bridge defects increases with increasing W_y/W_x. As demonstrated in Fig. 7, increasing the boundary anchoring strength $\epsilon_{GB\text{-}LJ}$ will suppress the appearance of the bridge defect pattern. This tendency is still kept, even when $\epsilon_{GB\text{-}LJ} = 15.0\epsilon_0$. Thus, compared to the square confinement systems, the relative stability of defect patterns in rectangle confinement boundaries is more sensitive to the boundary anchoring strength.

IV. CONCLUSIONS

In summary, we perform a systematic study on the transition kinetics of defect patterns in confined two-dimensional smectic Gay-Berne liquid crystals using molecular dynamics simulations. We observe that the smectic layers tend to form typical bridge and diagonal defect patterns to satisfy the confinement boundary conditions. Due to the competition between neighboring and opposite boundary effects, these two defect patterns can be transformable continuously between each other over time. We further show that the relative stability of these two defect patterns can be controlled by properly tuning the confinement conditions. This work provides the basis for understanding the transition kinetics of defect patterns in confined smectic liquid crystals, possibly expanding the design of new liquid crystal materials for various technological applications.

[1] M. Barón, Pure Appl. Chem. **73**, 845 (2001).

[2] Y. Kawata, T. Yamamoto, H. Kihara, and K. Ohno, ACS Appl. Mater. Interfaces **7**, 4185 (2015).

[3] Y. Jin, S. J. Elston, J. A. J. Fells, M. J. Booth, C. Welch, G. H. Mehl, and S. M. Morris, Phys. Rev. Appl. **14**, 024007 (2020).

[4] E. Bukusoglu, M. B. Pantoja, P. C. Mushenheim, X. Wang, and N. L. Abbott, Annu. Rev. Chem. Biomol. Eng. **7**, 163 (2016).

[5] M. Peccianti, C. Conti, G. Assanto, A. De Luca, and C. Umeton, Nature (London) **432**, 733 (2004).

[6] E.-K. Fleischmann and R. Zentel, Angew. Chem. Int. Ed. **52**, 8810 (2013).

[7] J. T. Sun, L. H. Ren, K. L. Deng, T. Wang, Q. Guo, J. X. Sang, Y. Liu, H. Liu, J. H. Shang, and V. G. Chigrinov, Liq. Cryst. **46**, 1340 (2019).

[8] A. Eremin, R. Stannarius, S. Klein, J. Heuer, and R. M. Richardson, Adv. Funct. Mater. **21**, 556 (2011).

[9] M. González-Pinto, Y. Martínez-Ratón, and E. Velasco, Phys. Rev. E **88**, 032506 (2013).

[10] M. Robinson, C. Luo, P. E. Farrell, R. Erban, and A. Majumdar, Liq. Cryst. **44**, 2267 (2017).

[11] X. Yao, H. Zhang, and J. Z. Y. Chen, Phys. Rev. E **97**, 052707 (2018).

[12] Y. Hu, L. Hong, and W. Deng, Phys. Rev. E **98**, 032706 (2018).

[13] J. Walton, N. J. Mottram, and G. McKay, Phys. Rev. E **97**, 022702 (2018).

[14] G. D. Wall and D. J. Cleaver, Phys. Rev. E **56**, 4306 (1997).

[15] M. Melle, M. Theile, C. K. Hall, and M. Schoen, Int. J. Mol. Sci. **14**, 17584 (2013).

[16] M. Moradi and S. Hashemi, Eur. Phys. J. B **84**, 289 (2011).

[17] R. Busselez, C. V. Cerclier, M. Ndao, A. Ghoufi, R. Lefort, and D. Morineau, J. Chem. Phys. **141**, 134902 (2014).

[18] J. A. Moreno-Razo, E. J. Sambriski, N. L. Abbott, J. P. Hernández-Ortiz, and J. J. de Pablo, Nature (London) **485**, 86 (2012).

[19] S. Hashemi, Braz. J. Phys. **49**, 321 (2019).

[20] K. Sentker, A. W. Zantop, M. Lippmann, T. Hofmann, O. H. Seeck, A. V. Kityk, A. Yildirim, A. Schönhals, M. G. Mazza, and P. Huber, Phys. Rev. Lett. **120**, 067801 (2018).

[21] M. R. Khadilkar and A. Nikoubashman, Soft Matter **14**, 6903 (2018).

[22] M. Rahimi, H. Ramezani-Dakhel, R. Zhang, A. Ramirez-Hernandez, N. L. Abbott, and J. J. de Pablo, Nat. Commun. **8**, 15064 (2017).

[23] S. Schlotthauer, R. A. Skutnik, T. Stieger, and M. Schoen, J. Chem. Phys. **142**, 194704 (2015).

[24] L. B. G. Cortes, Y. Gao, R. P. A. Dullens and D. G. A. L. Aarts, J. Phys.: Condens. Matter **29**, 064003 (2017).

[25] G. Nyström, M. Arcari, and R. Mezzenga, Nat. Nanotechnol. **13**, 330 (2018).

[26] Y. Li, J. J.-Y. Suen, E. Prince, E. M. Larin, A. Klinkova, H. Thérien-Aubin, S. Zhu, B. Yang, A. S. Helmy, O. D. Lavrentovich, and E. Kumacheva, Nat. Commun. **7**, 12520 (2016).

[27] Y. Zhou, E. Bukusoglu, J. A. Martínez-González, M. Rahimi, T. F. Roberts, R. Zhang, X. Wang, N. L. Abbott, and J. J. de Pablo, ACS Nano **10**, 6484 (2016).

[28] T. Araki, F. Serra, and H. Tanaka, Soft Matter **9**, 8107 (2013).

[29] R. Ozaki, T. Matsui, M. Ozaki, and K. Yoshino, Appl. Phys. Lett. **82**, 3593 (2003).

[30] X. Wang, D. S. Miller, E. Bukusoglu, J. J. de Pablo, and N. L. Abbott, Nat. Mater. **15**, 106 (2016).

[31] M. Harada, M. Hirotani, and M. Ochi, J. Appl. Polym. Sci. **136**, 47891 (2019).

[32] A. Suh, M.-J. Gim, D. Beller, and D. K. Yoon, Soft Matter **15**, 5835 (2019).

[33] S. S. Lee, B. Kim, S. K. Kim, J. C. Won, Y. H. Kim, and S.-H. Kim, Adv. Mater. **27**, 627 (2015).

[34] M. Kleman and J. Friedel, Rev. Mod. Phys. **80**, 61 (2008).

[35] T. B. Saw, A. Doostmohammadi, V. Nier, L. Kocgozlu, S. Thampi, Y. Toyama, P. Marcq, C. T. Lim, J. M. Yeomans, and B. Ladoux, Nature (London) **544**, 212 (2017).

[36] I. Chuang, R. Durrer, N. Turok, and B. Yurke, Science **251**, 1336 (1991).

[37] M. González-Pinto, Y. Martínez-Ratón, E. Velasco, and S. Varga, Phys. Chem. Chem. Phys. **17**, 6389 (2015).

[38] C. Chiccoli, L. R. Evangelista, P. Pasini, G. Skačej, R. T. de Souza, and C. Zannoni, Sci. Rep. **8**, 2130 (2018).

[39] E. Cañeda-Guzmán, J. A. Moreno-Razo, E. Díaz-Herrera, and E. J. Sambriski, Mol. Phys. **112**, 1149 (2014).

[40] V. Palacio-Betancur, J. C. Armas-Pérez, S. Villada-Gil, N. L. Abbott, J. P. Hernández-Ortiz, and J. J. de Pablo, Soft Matter **16**, 870 (2020).

[41] G. P. Alexander, Bryan Gin-ge Chen, E. A. Matsumoto, and R. D. Kamien, Rev. Mod. Phys. **84**, 497 (2012).

[42] D. J. Gardiner, S. M. Morris, and H. J. Coles, Sol. Energy Mater. Sol. Cells **93**, 301 (2009).

[43] K. Li, M. Pivnenko, D. Chu, A. Cockburn, and W. O'Neill, Liq. Cryst. **43**, 735 (2016).

[44] H.-Y. Chen and J.-S. Wu, J. Soc. Inf. Disp. **18**, 415 (2010).

[45] E. A. Büyüktanir, M. Mitrokhin, B. Holter, A. Glushchenko, and J. L. West, Jpn. J. Appl. Phys. **45**, 4146 (2006).

[46] M. Date, Y. Takeuchi, and K. Kato, J. Phys. D: Appl. Phys. **32**, 3164 (1999).

[47] Z. Dogic and S. Fraden, Phys. Rev. Lett. **78**, 2417 (1997).

[48] F. Serafin, M. J. Bowick, and S. R. Nagel, Eur. Phys. J. E **41**, 143 (2018).

[49] M. Salamonczyk, J. Zhang, G. Portale, C. Zhu, E. Kentzinger, J. T. Gleeson, A. Jakli, C. De Michele, J. K. G. Dhont, S. Sprunt, and E. Stiakakis, Nat. Commun. **7**, 13358 (2016).

[50] T. Geigenfeind, S. Rosenzweig, M. Schmidt, and D. de las Heras, J. Chem. Phys. **142**, 174701 (2015).

[51] R. F. Zhang, C. L. Ren, J. W. Feng, and Y. Q. Ma, Sci. China: Phys., Mech. Astron. **62**, 117012 (2019).

[52] L. Onsager, Ann. N.Y. Acad. Sci. **51**, 627 (1949).

[53] X. Zhu, T. M. Truskett, and R. T. Bonnecaze, Soft Matter **15**, 4162 (2019).

[54] Z.-W. Li, Y.-L. Zhu, Z.-Y. Lu, and Z.-Y. Sun, Soft Matter **14**, 7625 (2018).

[55] M. A. Bates and G. R. Luckhurst, J. Chem. Phys. **110**, 7087 (1999).

[56] E. de Miguel, E. M. del Río, and F. J. Blas, J. Chem. Phys. **121**, 11183 (2004).

[57] G. R. Luckhurst and P. S. J. Simmonds, Mol. Phys. **80**, 233 (1993).

[58] See Supplemental Material at http://link.aps.org/supplemental/10.1103/PhysRevE.104.044704 for typical defect patterns in square and rectangle confinements, and time evolution of the orientational order parameters.

[59] Y.-L. Zhu, H. Liu, Z.-W. Li, H.-J. Qian, G. Milano, and Z.-Y. Lu, J. Comput. Chem. **34**, 2197 (2013).

[60] Z.-W. Li, L.-J. Chen, Y. Zhao, and Z.-Y. Lu, J. Phys. Chem. B **112**, 13842 (2008).

[61] S. I. Hernández, J. A. Moreno-Razo, A. Ramírez-Hernández, E. Díaz-Herrera, J. P. Hernández-Ortiz, and J. J. de Pablo, Soft Matter **8**, 1443 (2012).

[62] M. P. Allen and D. J. Tildesley, *Computer Simulation of Liquids* (Clarendon, Oxford, 1987).

[63] D. C. Rapaport, *The Art of Molecular Dynamics Simulation*, 2nd ed. (Cambridge University Press, New York, 2004).

[64] R. Berardi, A. P. J. Emerson, and C. Zannoni, J. Chem. Soc., Faraday Trans. **89**, 4069 (1993).

[65] U. Fabbri and C. Zannoni, Mol. Phys. **58**, 763 (1986).

[66] Z.-W. Li, Y.-L. Zhu, Z.-Y. Lu, and Z.-Y. Sun, Soft Matter **10**, 5472 (2014).

[67] D. Frenkel and B. Smit, *Understanding Molecular Simulation: From Algorithms to Applications*, 2nd ed. (Academic, San Diego, 2002).